

Given the importance of the dissolved oxygen (DO) concentration in aquatic ecosystems, scientists and natural resource management agencies rely heavily upon in situ observations of DO to understand, interpret, and manage physical properties and biological resources in marine and freshwater environments. Previous studies have assumed that 2D depth profiles of DO are sufficient to characterize the variability in DO that may affect local ecosystems. Here the necessity for *higher-resolution* estimation of DO variations in a 3D volume of water is explored. To accomplish this goal, a method is proposed that uses repeated deployments of AUV missions to quantify the temporal dynamics of DO and calculate an oxygen budget for a water body in four dimensions.

This paper presents and demonstrates a new approach to investigating and quantifying the distribution and spatial heterogeneity DO in three dimensions of a defined water volume using an autonomous underwater vehicle (AUV). Furthermore, a method is proposed that uses repeated deployments of AUV missions to quantify the temporal dynamics of DO and calculate an oxygen budget for a water body in four dimensions.

To accomplish this, a new, fast-responding sensor that measures DO concentration in percentage of saturation, from which DO in absolute units can be calculated, was integrated into an AUV. A Kalman filter-based strategy for fusing DO measurements is also presented that constructs a time series of 3D DO estimates. What follows in Section 2 is an overview of other work in which an AUV was used to measure underwater ecosystem indicators. In Section 3, the hardware components are described. The method used for calculating DO estimates is shown in Section 4. The field trials used to validate the approach and the corresponding results are presented in Sections 5 and 6, respectively. Finally, conclusions are drawn in Section 7.

2. RELATED METHODS FOR SAMPLING DISSOLVED OXYGEN

Traditional methods for measuring DO are chemical analyses (e.g., Winkler titration), stable isotope techniques, or electrochemical sensors (e.g., Clark-type sensors). Recently, optical technologies have been applied and developed for in situ measurements of DO (Glud, Gundersen, & Ramsing, 2000; Tengberg et al., 2006). In fact, a novel compact, robust, and fast-responding optical DO sensor is now commercially available: the Aanderaa 4330F oxygen optode (Aanderaa Data Instruments [AADI], 2010), which can deliver in situ oxygen concentration data with high accuracy and temporal resolution.

The Aanderaa optode sensor makes an optical measurement by exciting a luminiferous porphyrin foil with a monochromatic pulse of light from a light-emitting diode (LED). The quenching time of the emitted fluorescence is

dependent on the DO concentration in the medium (Tengberg et al., 2006).

Another recent approach for estimating DO concentrations and flux rates take advantage of the *eddy-correlation* technique, relying on simultaneous measurements of the fluctuating vertical velocity and oxygen concentration above the seafloor (Berg et al., 2003). The technique has been used to measure DO flux rates across the benthic-pelagic interface, i.e., between the seafloor communities and the overlying water, with a high temporal resolution, for instance, in seagrass meadows (Hume, Berg, & McGlathery, 2011). There is a potential to combine the method presented here with the eddy-correlation technique for systematically studying DO dynamics in confined aquatic ecosystems and to set up integrated system budgets of oxygen or carbon turnover.

Autonomous platforms equipped with relevant sensors afford limnologists and oceanographers unprecedented sampling opportunities (Dickey, Itsweire, Moline, & Perry, 2008). Aquatic environments remain grossly undersampled and are often difficult and time-consuming to sample because of limited access (e.g., rough weather, far from ports, under ice) and vast spatial distribution (both horizontally and vertically). However, autonomous vehicles are capable of providing high-resolution survey data in both the horizontal and vertical dimensions (Moline, Blackwell, et al., 2005; Dickey et al., 2008). Relative to previous methods, these surveys are fast and low-cost.

Some examples of current autonomous underwater platforms include remote environmental monitoring units (REMUS) (Allen et al., 1997; Moline, Blackwell, et al., 2005), SAUV II (Blidberg et al., 2005; Crimmins et al., 2005), and the Slocum Glider (Webb, Simonetti, & Jones, 2001). The REMUS is propeller-driven and steered using vertical and horizontal fins attached to the back of the body. It has had a variety of applications, e.g. testing bioluminescence in the San Diego Bay for applications of tracking objects moving through the ocean (Moline, Bissett, et al., 2005). The SAUV II is a solar-powered AUV that can charge batteries at the water's surface and utilize that charge for up to 12 h. It uses a single vectored thruster at the rear of the AUV for locomotion. This device has been used to measure DO levels in Greenwich Bay, RI to test for hypoxic water (Crimmins et al., 2005). The Slocum Glider is an energy-efficient AUV that uses a buoyancy engine in conjunction with fixed wings and controlled redistribution of internal mass to create motion in the horizontal direction while controlling their position. In (Leonard et al., 2007), collaborative vehicle control algorithms were presented for multiple gliders performing an adaptive sampling task.

Previous studies using AUVs to sample oceanographic data have proven their effectiveness in the field (Moline, Blackwell, et al., 2005). Dissolved oxygen was not the only variable measured; temperature, salinity, depth, bathymetry, and bioluminescence are some other examples

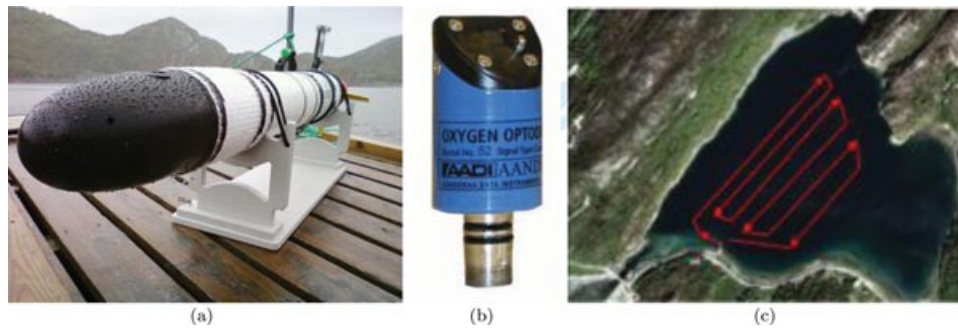


Figure 1. (a) The OceanServer Iver2 AUV, (b) the oxygen optode (4330F) that was mounted on the Iver2, and (c) the prescribed path for the AUV in Hopavågen Bay, Norway.

of data that are currently being measured using AUVs. AUV data sampling can be much more effective than previous methods because of their small size, lower cost, and ability to collaborate in groups to cover large areas quickly. Crimmins et al. (2005) state that towed sampling devices are problematic because of vessel draft and sediment disturbance in shallow waters, whereas a smaller AUV has less impact on surrounding waters. Jenkins et al., (2010) demonstrated the use of an AUV for obtaining DO measurements (as well as temperature, salinity, light attenuation, and seabed topography maps) while navigating below the Pine Island Glacier ice shelf in Antarctica. Additionally, using multiple AUVs for sampling can result in faster task completion, greater sampling resolution, or greater sampling accuracy.

Examples of using AUVs for marine biology include (Moline et al., 2009), where coastal planktonic communities were studied using an onboard sensor. In (Grasmueck et al., 2007), the finding and mapping of coral mounds in Florida was presented. Chemical sampling with AUVs and appropriate sensors is discussed in (Camilli et al., 2004), and was a recently applied in the Deepwater Horizon oil spill, tracking the spill and evaluating the bacterial respiration by oxygen concentrations using an onboard mass spectrometer (Camilli et al., 2010). More recently, AUVs have been used to map benthic habitats (Williams, Pizarro, Jakuba, & Barrett, 2010).

For this effort, we exploited the benefits of an AUV integrated with an Oxygen Optode 4330F sensor that measures DO to carry out field investigations in Hopavågen Bay, Norway. Contributions of this work include

- Oxygen optode 4330F sensor integration into an AUV
- DO sensor modeling
- DO estimation techniques
- Calculation of total DO in a water volume
- Field experiment validation of techniques

Unlike previous work, this study demonstrates not only the importance of measuring and estimating DO in

three spatial dimensions, but also that it is necessary for accurately estimating DO quantities in a water volume.

3. HARDWARE SYSTEM

3.1. Autonomous Underwater Vehicle Platform

An OceanServer Iver2 AUV [Figure 1(a)] was used as the base platform for our investigations. The Iver2 has a length of 1.27 m and a diameter of 0.147 m and weighs 21 kg. It can dive to a maximum depth of 100 m and has a maximum speed of 2 m/s. For propulsion the Iver2 has one propeller with two horizontal and two vertical control surfaces. However, for this experiment, the Iver2's servo for the top control surface was damaged so the only the two horizontal and the bottom vertical control surfaces were available. The sensors that were already on the Iver2 include a compass, a depth sensor, an altimeter, a GPS, and an angle sensor for each control surface. The DO sensor was integrated onto the platform by the authors. This Iver2 contained two 500-MHz processors: the main computer and a secondary processor. The main computer is responsible for autonomous tracking of waypoints. Missions are created with OceanServer's software. The secondary processor, upon which Windows XP was installed, can communicate with the main processor via a serial port connection. In our studies the secondary processor was used to run software that logs the DO data.

3.2. Dissolved Oxygen Sensor

The Oxygen Optode 4330F sensor [Figure 1(b)] is manufactured by AADI (Aanderaa Data Instruments, Bergen, Norway). Its dimensions are 36×86 mm and the sensor measures temperature and dissolved oxygen concentration (in percentage of saturation, from which absolute concentrations can be calculated). The sensor measures DO in the medium using the lifetime-based luminescence quenching principle. It has no stirring sensitivity (does not consume oxygen), long-term calibration stability (>1 yr, according to the manufacturer), and a response time (63%) with the fast

response foil of <8 s. This response time allows sampling while the sensor is in motion. This is not to be confused with the sensor sampling rate of 1 Hz.

The sensor outputs data in two formats: RS-232 and CANbus AiCaP. The RS-232 connection was used to provide simplicity, and because of the possibility of integrating the sensor data directly into a custom control loop for the Iver2. The sensor outputs the DO as a percentage of atmospheric saturation between 0% and 150%, with a resolution of 0.4% and an accuracy of less than 5% within the calibrated range of 0% to 120%. For known salinity, the sensor outputs absolute DO concentrations between 0 and 500 μM , with a resolution of less than 1 μM and an accuracy of better than 8 μM or 5%, whichever is greater. As will be described, the DO as a % saturation can be converted to an absolute concentration if both temperature and salinity are known. The optode is slightly pressure-sensitive, with a linear suppression of the signal by 3.2% (1,000 dbar) $^{-1}$ (Uchida, Kawano, Kaneko, & Fukasawa, 2008). Consequently, we assumed that the pressure sensitivity of the optode was negligible in this study because operations were conducted at depths of less than 15 m.

3.3. System Integration

Three cables were designed to integrate the Oxygen Optode sensor with the secondary processor on the Iver2. Cable 1 brought 12 V of power to the sensor. Cable 2 interfaced with one of the serial ports on the secondary processor. Cable 3 provided a bridge between the Iver2's CPU area (water-tight) and the Iver2's cable cavity. The sensor's cable connected to cable 3 in the Iver2's cable cavity and from there went outside to connect to the sensor. Once the sensor was connected to the secondary processor of the Iver2, the software provided by AADI was run on the secondary processor to log all the data coming in from the sensor.

4. DISSOLVED OXYGEN ESTIMATION

4.1. Dissolved Oxygen Lattice Model

In this work, the underwater environment is described as a 3D lattice structure (i.e., a grid) that is fixed in space with respect to the environment, and is denoted here as L . Each lattice point $l_{i,j,k}$ of L uses three, indices (i, j, k) as a reference for its location within the lattice (see Figure 2):

$$L(m) = \{l_{i,j,k}(m) | i \in [1, I], j \in [1, J], k \in [1, K]\}. \quad (1)$$

Lattice points are characterized by a 3D position $[x \ y \ z]$ in an inertial coordinate frame fixed in the underwater environment of interest, a DO estimate o for the lattice point location, and the corresponding error variance σ_o^2 of the DO estimate. Because DO is time-varying, the DO estimates are a function of the discrete variable m , representing a step in a time series. In this work, a relatively low resolution of time is used because DO only varies significantly across several hours (e.g., in a series of four time steps, $m = 0$ corresponds

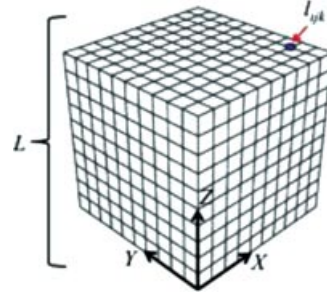


Figure 2. The lattice structure L anchored to a fixed underwater environment with a Cartesian coordinate frame labeled XYZ . A lattice point $l_{i,j,k}$ (i.e., a node in the lattice), uses the three indices i, j, k as references for its position in the lattice.

to estimates at time 0 h, $m = 1$ to a time 3 h later, $m = 2$ to a time 6 h later, $m = 3$ to a time 9 h later):

$$l_{i,j,k}(m) = [x \ y \ z \ o(m) \ \sigma_o^2(m)]_{i,j,k}. \quad (2)$$

In this model, the spacing between lattice points was selected, which determined the sizes of I, J, K necessary for the water volume of interest. The goal of this research was to determine the DO in $\mu\text{mol/L}$ for each lattice point, $o_{i,j,k}(m)$, and the corresponding error variance, $\sigma_{o,i,j,k}^2(m)$.

Although DO at each lattice point is time-dependent, in this research it was assumed that DO variations in time were negligible within a single AUV mission deployment (approximately an hour in length). As shown later, DO can change significantly over time spans of several hours. For the field trials that follow, there are four AUV mission deployments that occurred several hours apart, and m corresponds to the AUV mission number (i.e., 1,2,3, or 4).

4.2. Conversion to Absolute Dissolved Oxygen Concentration

The oxygen optode measures DO as a saturation percentage. The absolute concentration o can be calculated as the product of measured DO saturation percentage z_o and oxygen solubility K_{sp} as follows:

$$o = z_o K_{sp}. \quad (3)$$

Absolute values of K_{sp} can be calculated knowing the exact temperature T and salinity S according to Garcia and Gordon (1992). In this study we used a simplified version (Eq. (4)) of their equation to calculate K_{sp} , which is accurate for temperature values between 0 and 10°C and salinity values between 25 and 35, both of which are valid ranges for the bay of interest being sampled:

$$K_{sp} = (-0.0017T^2 + 0.088T - 2.5696)S + 0.2215T^2 - 12.304T + 448.09. \quad (4)$$

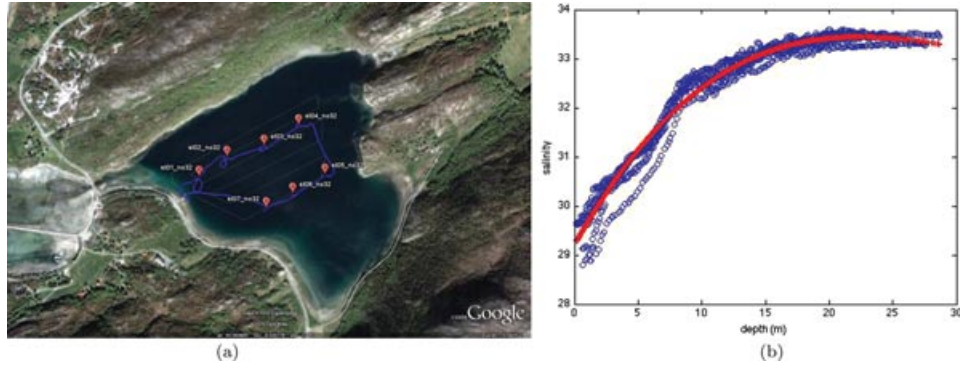


Figure 3. Salinity modeling. (a) The seven geographic locations from which salinity measurements were obtained. (b) The data obtained from all seven locations, with a polynomial fit model in red.

The oxygen optode measures temperature with every DO saturation measurement. Unfortunately, the Iver2 was not equipped with a salinity sensor, as would be standard for this measurement. For this work, a salinity sensor (CTD, Model SD204, SAIV AS, Bergen, Norway) was lowered by hand to various depths from a small boat. This was repeated at seven different locations across the Hopavågan bay. Figure 3(a) shows the seven locations across the bay from which measurements were obtained. As shown in Figure 3(b), the salinity S has minimal variance across the horizontal planes, but significant variance with depth. Hence, salinity was modeled as a function only of depth. In Figure 3(b), the relationship between salinity and depth is shown. A third-order polynomial was used to approximate the relationship between salinity and depth (the fit is illustrated as the red line). This will not be required for many AUVs that have an onboard salinity sensor.

For any given AUV location, the corresponding depth was used in combination with the model depicted in Figure 3(b) to calculate salinity. Hence, for every point in an AUV trajectory, measured salinity, temperature, and DO saturation percentage were available. By substituting these measurements into Eq. (3) and Eq. (4), absolute DO concentrations for each AUV location were calculated.

4.3. Sensor Fusion

To fuse multiple measurements of absolute DO concentration taken from multiple AUV positions, a 1D Kalman filter (KF) was used (Thrun, Burgard, & Fox, 2005). Each new DO measurement $z_{o,t}$ was assumed to be perturbed by random noise, which is modeled as a Gaussian distribution with zero mean and variance $\sigma_{z,t}^2$. Similarly, the absolute DO concentration \hat{o}_t calculated from such measurements using Eq. (3) and Eq. (4) was modeled as a Gaussian distribution with zero mean and variance $\sigma_{\hat{o},t}^2$.

To incorporate these new measurements into the estimate of absolute DO concentration for each grid point, the

Kalman gain can be calculated as

$$K_t = \frac{\sigma_{o,t-1}^2}{\sigma_{o,t-1}^2 + \sigma_{\hat{o},t}^2}. \quad (5)$$

Note that the subscript i, j, k has been removed for clarity. The subscript t indicates the time step within the AUV mission upon which a new DO measurement was obtained. In this case, time varied on the order of seconds between time steps. The new DO estimate for a grid point can then be calculated as

$$o_t = o_{t-1} + K_t(\hat{o}_t - o_{t-1}). \quad (6)$$

As well, the following equation can be used to calculate the corresponding DO estimate error variance:

$$\sigma_{o,t}^2 = (1 - K_t)\sigma_{o,t-1}^2. \quad (7)$$

4.4. Sensor Modeling

The KF assumes that absolute DO measurements are perturbed by zero-mean Gaussian noise with variance $\sigma_{\hat{o}}^2$. In the modeling of variance, it was assumed that the planar distance $\delta p_{i,j,k,t}$ and the vertical distance $\delta v_{i,j,k,t}$ between a lattice point and a measurement location would affect the confidence with which the measurement would reflect the actual DO at the lattice point. This assumption is based on that fact that the variables of interest typically vary much less in the horizontal plane than with depth:

$$\sigma_{\hat{o},t}^2 = \sigma_{p,t}^2(\delta p_{i,j,k,t}) + \sigma_{v,t}^2(\delta v_{i,j,k,t}) \quad (8)$$

$$\delta p_{i,j,k,t} = \sqrt{(x_t - x_{i,j,k})^2 + (y_t - y_{i,j,k})^2} \quad (9)$$

$$\delta v_{i,j,k,t} = \text{abs}(z_t - z_{i,j,k}). \quad (10)$$

Data from missions run in Hopavågan Bay were used for the sensor modeling. To determine the variance in absolute DO concentration as a function of planar

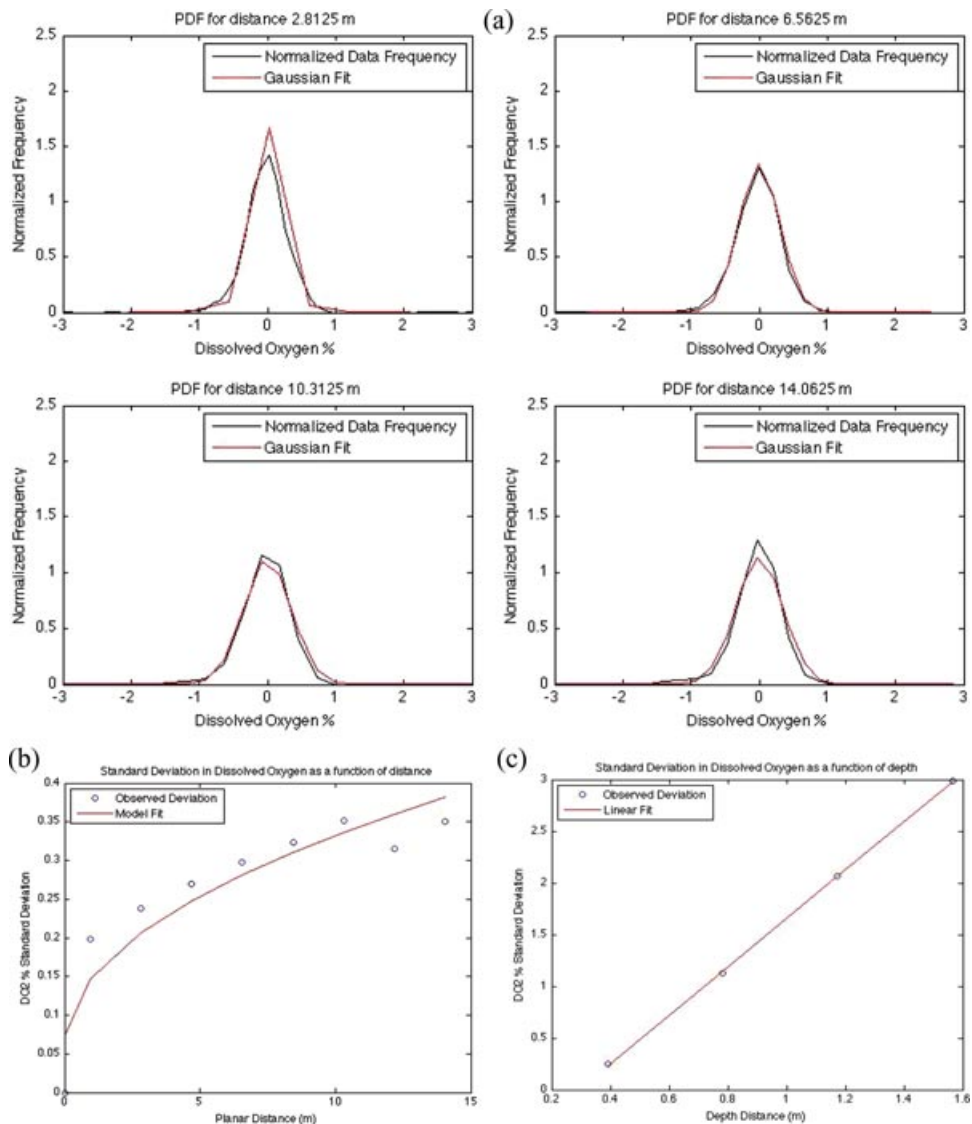


Figure 4. Sensor modeling. (a) Histograms, where the frequency is plotted as a function of difference between measurements. The four plots correspond to increasing planar distance between measurements. (b) The standard deviations calculated for each histogram in (a), fit with a linear least-squares model. (c) A similar model of standard deviation with increasing depth is shown.

distance, histograms for increasing planar distance were created in which the frequency of change in DO was plotted. Figure 4(a) shows the resulting histograms for planar distances of 2.81, 6.56, 10.31, and 14.06 m, respectively. From this figure, it can be seen that the distributions of change in DO resemble Gaussian distributions. Moreover, the variance increases with planar distance; i.e., the greater the distance at which a measurement is taken from a lattice point, the less confidence that the measurement represents the lattice point's true DO.

This increase in variance with planar distance was modeled linearly. Figure 4(b) shows the variances for the eight distributions including those in (a), along with a least-squares square-root fit. The same procedure was used to determine the increase in variance with change in depth, i.e., vertical distance (Figure 4(c)). It should be clear from the slopes of the plots in (b) and (c) that our confidence in a measurements ability to reflect a lattice point's DO is much more dependent on the difference in depth than on the planar distance.

5. FIELD INVESTIGATIONS

To validate the ability of the Iver2 to conduct DO sampling, a series of field investigations were conducted in Hopavågen Bay, Norway. The bay is essentially a closed system with high residence times for the water (low exchange). This makes it an ideal location for change detection, in this case to examine the net production of oxygen within the system (i.e., the sum of the oxygen production rate from photosynthesis and the oxygen consumption rate from respiratory activity and microbial mineralization). The location is sheltered from weather exposure and the advective forces were low. The water column was stratified in the upper 10 m, as also seen from the salinity profile, i.e., good for gas-exchange studies.

To best characterize the DO gradients throughout the bay, a variety of undulating lawnmower trajectories were tested. The trajectories were designed to cover the section of the bay that has minimum depth, and do so within a time span in which DO will not change significantly. The undulation frequency and the total trajectory time were the two major variables altered between tests. Table I lists the mission details for these experiments that were conducted within a 24-h period.

For the deployments described, a grid lattice spacing included a horizontal grid point separation of 20.0 m, with a vertical grid point separation of 2.0 m. The lattice had dimensions of $23 \times 29 \times 8$, resulting in 5,336 nodes. Hence, there were 23 nodes \times 29 nodes in each horizontal layer, and there were 8 layers.

Before measurements could be used to calculate the lattice DO state estimates, AUV position estimates were updated to account for the drift that occurs while the AUV is underwater and subjected to currents. At the surface, the AUV fuses compass, propeller speed, and GPS measurements to estimate the position of the AUV. This filtering is accomplished with OceanServer's state estimator, proprietary software that does not output state error covariances. Our experimentation has demonstrated that localization errors are similar to errors associated with the GPS measurements (on the order of 2–3 m, but bounded).

Once below the surface, the AUV only has access to compass and propeller speed. Hence, while it is submerged the horizontal position errors grow laterally with respect to forward motion. At worst, we observed a 25% error growth;

e.g., in 40 m of forward motion, the AUV's horizontal position estimate drifted laterally by 10 m from its actual position. During all dives, this error drift was consistent in terms of direction and relative magnitude, indicating the effects of a constant-velocity current. To account for this, subsurface state position estimates are calculated as the interpolated value between the location estimates just before and after the AUV dives.

Using the AUV position estimates, every single DO measurement obtained during the mission was used to update the DO estimate and associate error variance for *each* of the 5336 nodes. The sensor model described earlier gives higher confidence in measurements taken closer to the node location. Each measurement was fused with each node's DO estimate using the Kalman filter described previously.

6. RESULTS

Examples of the DO estimates calculated for our lattice structure are shown in Figures 5–7. Plotted in Figure 5 is the DO for each horizontal layer of lattice points. These layers are plotted for six different values of depth. The plots are also made for each of the four different missions, each conducted at a different time of day. It is notable that the system is capable of measuring variations in DO across both space and time. As expected, the highest DO gradient occurs with respect to depth, but horizontal gradients in DO are clearly visible. When the DO estimates are compared between missions, there is significant variation. Consider the depth = 4 m plots (upper right) in Figures 5(a)–5(d). These are the DO estimates for the same locations, but at different points in time. There are clear changes in DO as time progresses.

DO measurements at the beginning of the mission occur earlier (e.g., an hour) than DO measurements at the end of the mission. When measurements for a single lattice point are fused, the set of measurements taken most closely to the lattice point will contribute most to the DO estimate for that lattice point (according to our sensor model). Hence, the time stamp for each lattice point's DO estimate more closely matches the time the AUV was in close proximity the point location.

For these experiments, the DO measurements taken during a single mission are obtained within an hour of each

Table I. Experiments conducted in Hopavågen.

| Mission num. | Date | Start time | Trajectory type | Mission time (min) | Undulation depth (m) |
|--------------|---------------|------------|-----------------|--------------------|----------------------|
| 1 | June 19, 2010 | 6:23 | Surface | 127 | 0 |
| 2 | June 19, 2010 | 19:48 | Undulating | 75 | 10 |
| 3 | June 19, 2010 | 21:30 | Undulating | 68 | 10 |
| 4 | June 20, 2010 | 12:15 | Undulating | 70 | 10 |
| 5 | June 20, 2010 | 14:52 | Undulating | 76 | 10 |

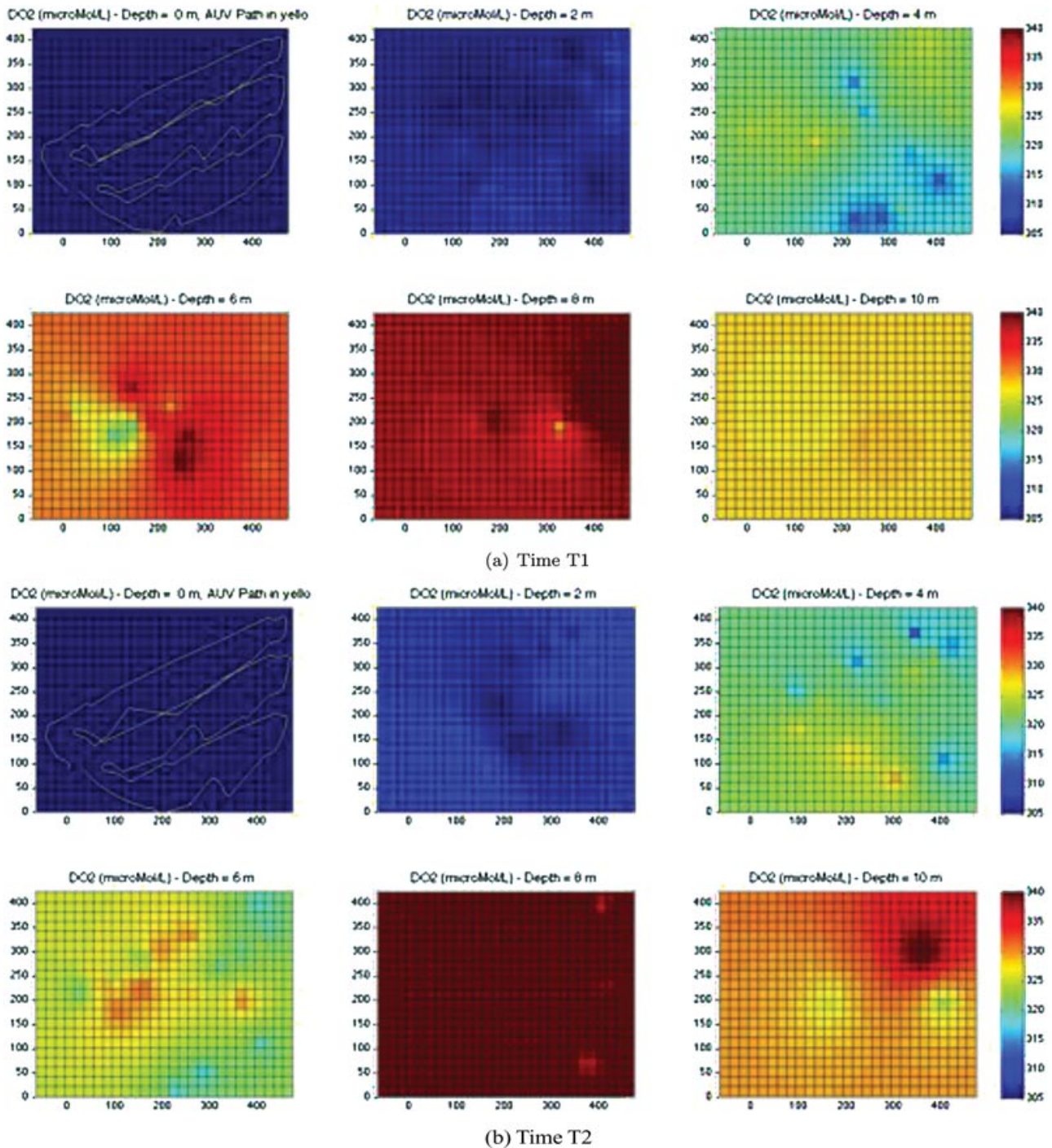
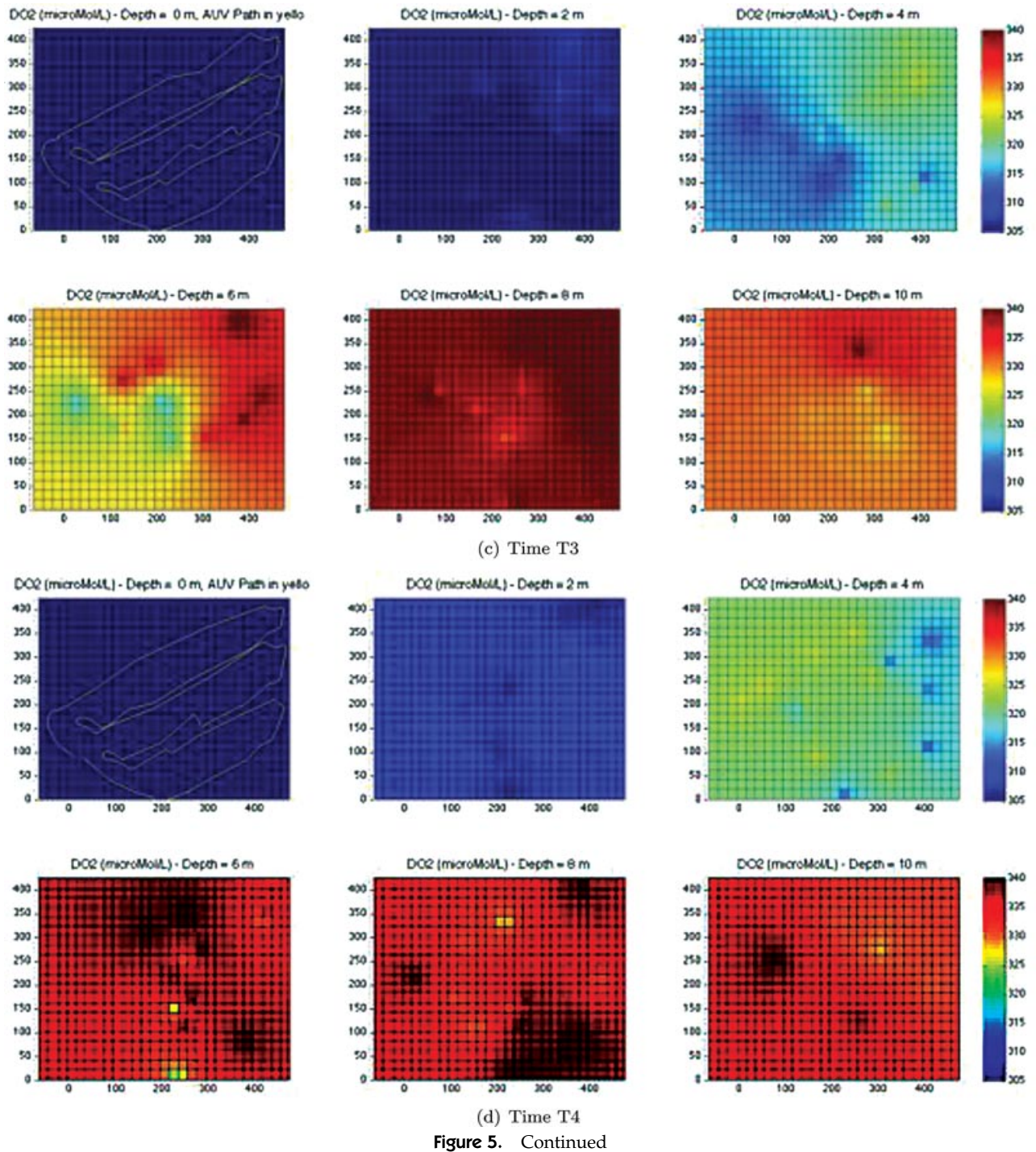


Figure 5. Planar results. Dissolved oxygen estimates for horizontal planes of the lattice are plotted for four field Deployments (a to d). For each deployment, six different depth levels of the lattice are plotted. The depth = 0 m plot also has the AUV trajectory for the mission plotted in yellow.



other. Because DO varies over a time scale of several hours, and time stamps of lattice point DO estimates are within an hour of each other, it is assumed that asynchronous measurement effects are not significant.

Also, without a DO sensor that has a fast response time, on the order of seconds, the AUV cannot traverse the desired path quickly and complete the mission within an hour. A fast sensor response is crucial to cover greater

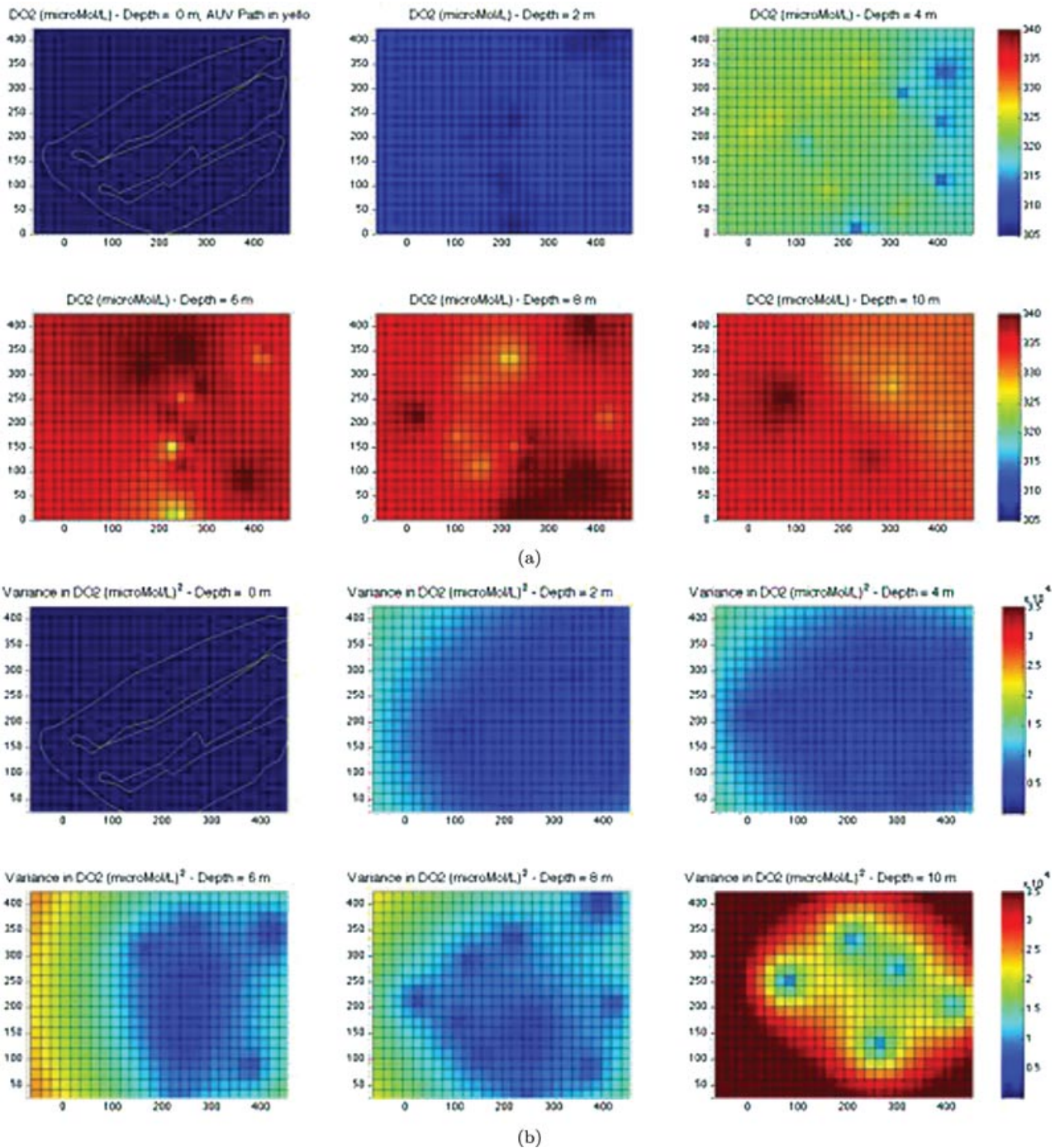


Figure 6. Planar error variance. The dissolved oxygen estimates for horizontal planes of the lattice are shown for the fourth deployment (a) along with the error variance for each grid point (b).

volumes of water but also is essential for resolving the spatial heterogeneity of DO, as a relatively slower sensor will *smooth* the amplitude of the DO measurements and thus decrease the spatial resolution.

Figure 6(a) illustrates the DO estimates at each node in the lattice, as estimated by fusing multiple measurements with the KF described in Section 4.3, with the corresponding error variance in DO, as determined by the KF shown

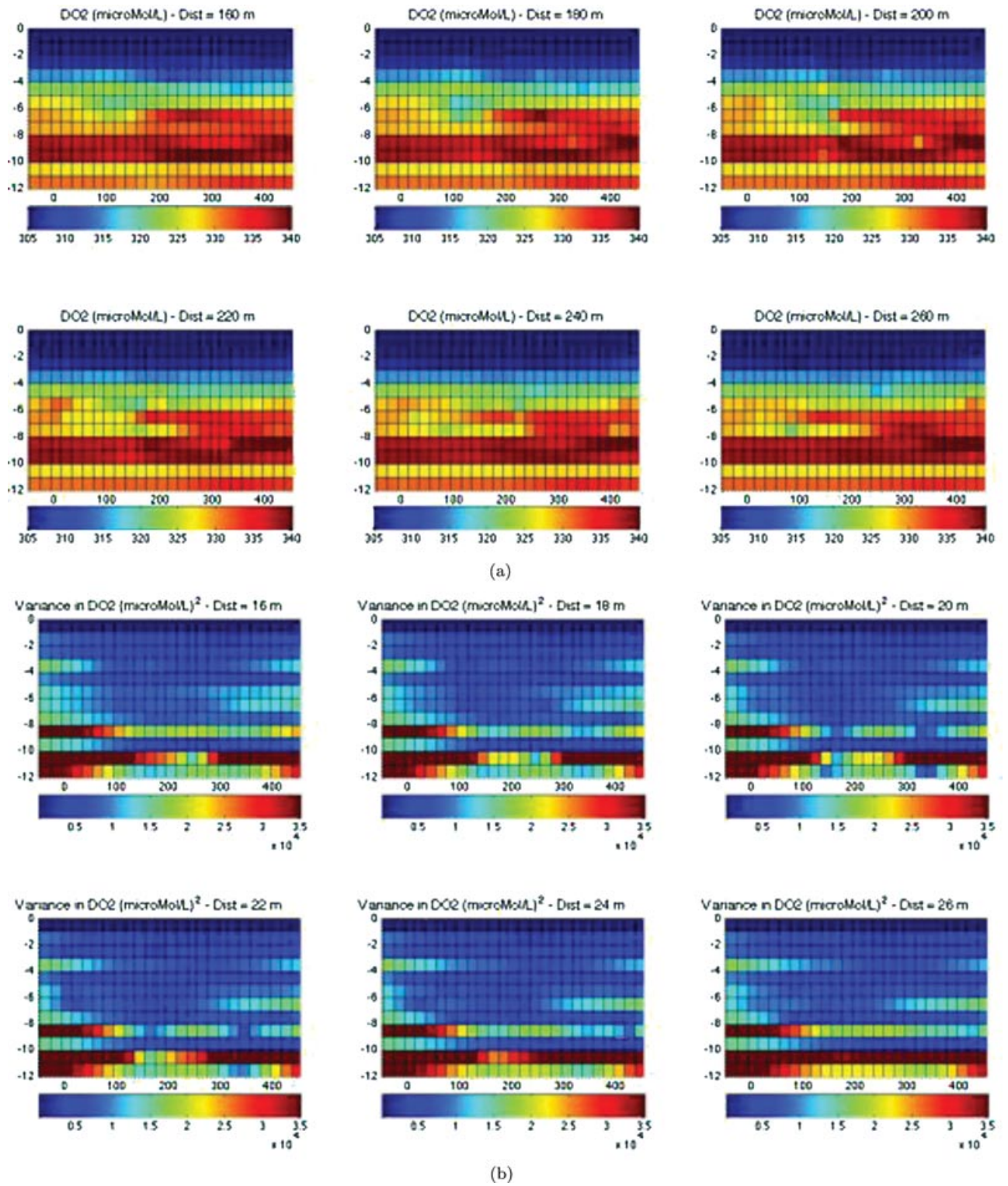


Figure 7. Depth plane profiles. The dissolved oxygen estimates for vertical planes of the lattice are shown in (a). In (b), the corresponding variance is plotted. Each plot is the YZ plane for particular values of X . For example, the Dist = 40 m subfigure corresponds to the plane located at $X = 40$ m in Figures 4 and 5.

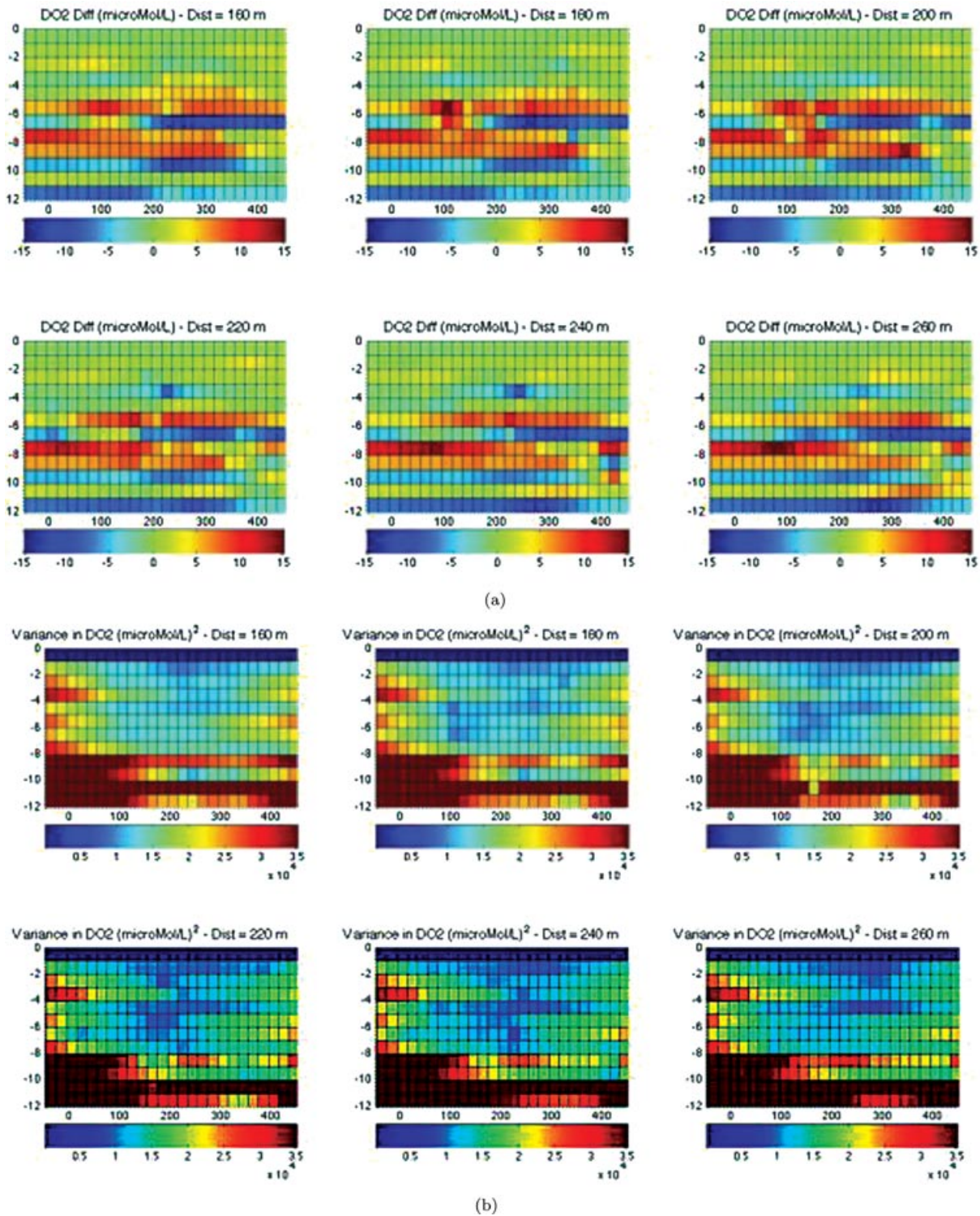


Figure 8. Depth profile differences over time. The differences of dissolved oxygen estimates between the second and third deployments. For vertical planes of the lattice, the differences between DO are plotted in (a). The corresponding error variance plots are shown in (b). In both (a) and (b), various vertical cross sections are shown where the Dist value in meters dictates the X value for the plotted YZ plane.

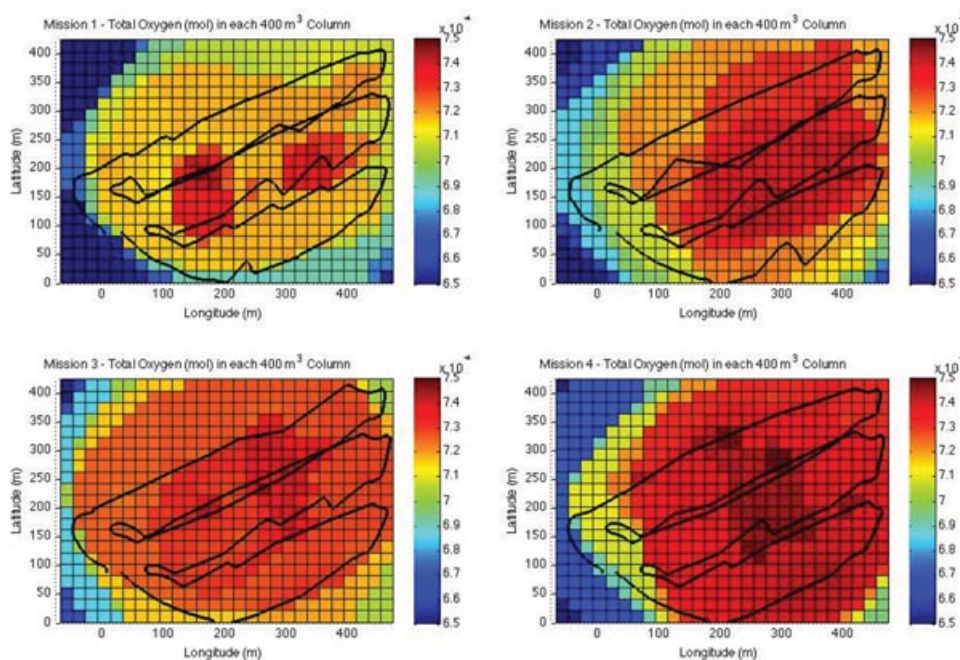


Figure 9. Total DO in each cell's water column of the investigated volume of water. By summing the DO of each node of the lattice, and knowing the distance between nodes in the lattice, the total DO can be calculated for each vertical column the bay water. Here, the total DO is plotted for each column, i.e., the total DO below the surface of each cell in the grid. Each of the four plots corresponds to a different mission deployment.

in Figure 6(b). In these plots, dark blue indicates low error variance, and it can be seen that error variance increases for nodes farther away from the AUV trajectory. This makes sense, as we have lower confidence in our DO estimates at locations where the AUV did not sample. As well, the error variance increases with depth, because fewer measurements were obtained at deeper positions in the bay. This is highlighted by the five clearly visible patches of low error variance (blue) where the AUV actually dove to depths of 10 m, in contrast to high error variance elsewhere.

In Figure 7(a), several vertical cross sections of the lattice structure DO estimates are shown. Each vertical cross section is an YZ plane for particular values of X . That is, the $\text{Dist} = 40$ m subfigure corresponds with the plane located at $X = 40$ m in Figures 4 and 5.

In Figure 7(b), the corresponding error variance as calculated with the filter described in Section 4.3 is shown. It is clear in Figure 7(a) that DO increases with depth, although an interesting feature is observed in the middle of the first three images, where a lower DO is observed even at slightly greater depths. In Figure 7(b), higher error variance is observed at the right and left sides of the images. This results from the facts that the AUV did not travel to these locations to obtain measurements and that the filter produces higher error variances with increasing distance between measurement and lattice node position (see the Gaussian sensor model shown in Section 4.4).

To exemplify the temporal variance in DO, the DO estimates for nodes in vertical cross sections of the lattice can be subtracted between different missions. In Figure 8(a), the DO as estimated for field trial 2 is subtracted from that estimated in field trial 3. Although many of the DO estimates do not seem to vary between the two experiments (as shown by the light green color), there are clear differences.

Consider the large positive difference (indicated by red) at a location of $(60, -9)$ in the bottom right plot ($\text{Dist} = 260$ m). If one observes the error variance, Figure 8(b) at that same location, it is clear there is high error variance at that location, leading us not to have much confidence in this difference. The large error variance for a lattice point is an indication that fewer measurements were obtained near the lattice point position.

However, consider the horizontal layer centered at $(100, -5.5)$ in the top three figures. The corresponding error variance shown in Figure 8(b) for this location is low, indicating high confidence that there is in fact a difference. That is, we believe there was a large change in DO at this location between experiments 3 and 2 (i.e., $15 \mu\text{M}$ in approximately 2 h).

To illustrate the DO changes across time, Figure 9 presents the sum of total DO in each vertical column of the area sampled. The four plots show increasingly more DO per vertical column, indicated by darker red shading.

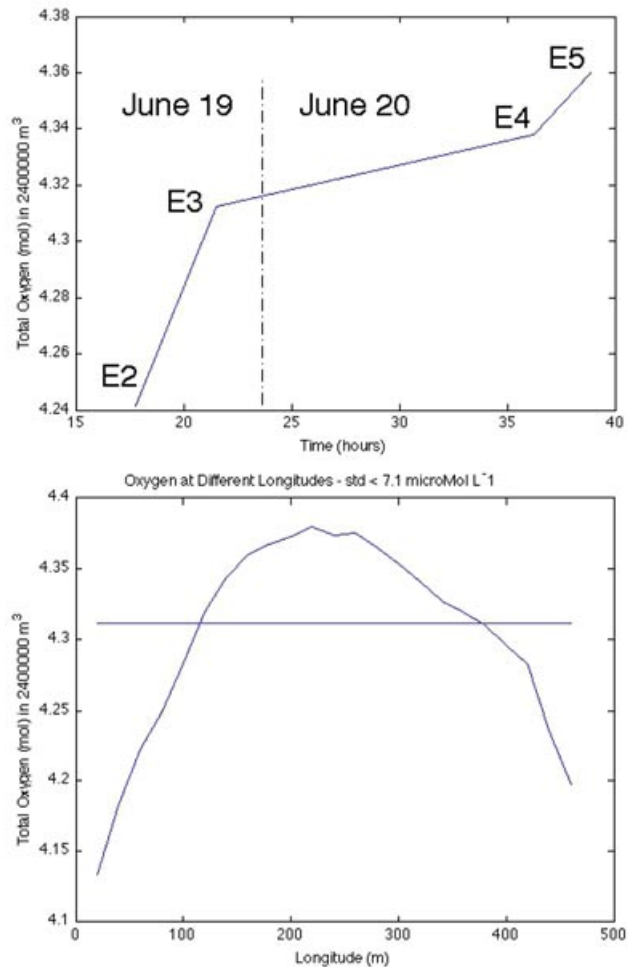


Figure 10. Total DO in the investigated volume of water. By summing the DO of each node of the lattice, and knowing the distance between nodes in the lattice, the total DO can be calculated for a particular volume of the bay water. In (a), the total DO is plotted as a function of mission number/time. In (b), one can see the total DO calculated based on vertical planes at different longitudes for mission 3. The total DO calculated by the volumetric approach for mission 3 is represented by the horizontal line.

This is further illustrated in Figure 10, where the total DO is plotted for each of the four subsurface field trials, labeled E2, E3, E4, and E5. The totals were calculated for each field trial by summing the DO over all grid cells with a minimum level of confidence (i.e., a maximum allowed error variance of $(0.00015 \mu\text{mol/L})^2$). Because each field trial's total DO was with respect to a slightly different volume (due to a different number of cells meeting the error variance criterion), each total was then normalized to be with respect to the approximate average volume of $2.4 \times 10^6 \text{ m}^3$.

Figure 10(b) shows the total DO for experiment 3 by summing over the cells for each longitude and then normalizing with respect to the same volume of $2.4 \times 10^6 \text{ m}^3$. That is, the total DO is calculated using only estimates from grid points in each vertical plane (e.g., Figure 7). As can be observed, higher DO totals are estimated when the longitudes corresponding to the central parts of the bay are considered. This is because the central bay has higher DO than along the edges. The large variance in DO as a function of longitude stresses the strength of obtaining a high-resolution 3D model of the bay, as opposed to a one-dimensional profile as commonly used in classical aquatic studies, when estimating total DO and its temporal dynamics.

7. CONCLUSION

This work has demonstrated a new way to create high-resolution estimates DO concentrations in an aquatic environment. The approach of mounting a new fast-responding oxygen optode on an AUV to obtain DO measurements across three spatial dimensions and time proved successful. As well, a simple KF-based approach to DO estimation of nodes in a 3D lattice was presented. The KF requires that measurements be modeled with a Gaussian distribution, which is shown to be a valid model for this sensor. The system is able to detect fine variations in DO across the four dimensions. The KF method also produces DO error variance for each lattice node position, providing a method for assessing confidence. Finally, by summing DO across the 3D lattice of grid cells with low error variance, the total DO in a particular water volume is calculated and shown to improve results when compared with similar calculations using only 2D vertical planes. This new method of quantifying the DO in a particular volume of water could be used as a measurement of the health of an ecosystem, evaluating net primary productivity, allowing the assessment of the impacts of fish farms, pollution, natural disasters, etc. This quantification could also be generalized to quantify the amount of several other dissolved gases and other substances that can be measured from compact electrochemical or optical sensors (e.g., colored dissolved organic matter) in aquatic environments.

To address the issue of obtaining DO measurements at different times within a single mission, further work could include multiple AUVs within a single mission. This work could also be extended to incorporate intelligent AUV path planning (Petres et al., 2007). There are earlier examples of AUV path planning for area coverage (Carroll et al., 1992), and more recent work has demonstrated onboard adaptive planning (Wang, 2007) as well as task planning (Chow, Huissoon, & Clark, 2011). More relevant are (Binney, Krause, & Sukhatme, 2010) and (Davini, Choboter, & Clark, 2011), where the authors used path planning to construct paths that maximized information gain. Such methods could be used in conjunction with the DO estimator to minimize error variance.

ACKNOWLEDGMENTS

The authors would like to acknowledge support by faculty and staff at the Trondheim Biological Station (TBS), Norway, who hosted researchers from Cal Poly. This expedition was partially funded by Cal Poly's Instructional Related Activities program. We would also like to thank Inga Aamot and Torunn B. Hancke for valuable assistance during pilot studies and data sampling. Professor J. Berge is acknowledged for financial support for the O₂ sensor and the Norwegian Research Council/NESSAR NFR# 176057/S30 is acknowledged for funding to KH. Finally, Professor G. Johnsen, partners, and contributors of the NORUS project (www.norus-science.com) are acknowledged for making the field work possible.

REFERENCES

- Aanderaa Data Instruments [AADI] (2010). Aanderaa 4330f oxygen optode.
- Allen, B., Stokey, R., Austin, T., Forrester, N., Goldsborough, R., Purcell, M., & von Alt, C. (1997, October). Remus: A small, low cost AUV; system description, field trials and performance results. In OCEANS '97. MTS/IEEE Conference Proceedings, Halifax, NS (Vol. 2, pp. 994–1000).
- Berg, P., Rowy, H., Janssen, F., Meyer, V., Jorgensen, B., Huettel, M., & de Beer, D. (2003, October). Oxygen uptake by aquatic sediments measured with a novel non-invasive eddy-correlation technique. *Marine Ecology Progress Series*, 261, 75–83.
- Binney, J., Krause, A., & Sukhatme, G. (2010, May). Informative path planning for an autonomous underwater vehicle. In Proceedings of IEEE International Conference on Robotics and Automation (ICRA), Anchorage, Alaska (pp. 4791–4796).
- Blidberg, D., Mupparapu, S., Chappell, S., Komerska, R., Jalbert, J., & Nitzelm, R. (2005, September). The SAUV II (solar powered AUV) test results 2004. In Oceans 2005—Europe, Washington, DC (Vol. 1, pp. 545–550).
- Camilli, R., Bingham, B., Jakuba, M., Singh, H., & Whelan, J. (2004, November). Integrating in-situ chemical sampling with auv control systems. In Oceans '04. MTS/IEEE Techno-Ocean '04, Kobe, Japan (Vol. 1, pp. 101–109).
- Camilli, R., Reddy, C. M., Yoerger, D. R., Van Mooy, B. A. S., Jakuba, M. V., Kinsey, J. C., McIntyre, C. P., Sylva, S. P., & Maloney, J. V. (2010). Tracking hydrocarbon plume transport and biodegradation at deepwater horizon. *Science*, 330(6001), 201–204.
- Carroll, K., McClaran, S., Nelson, E., Barnett, D., Friesen, D., & William, G. (1992, June). AUV path planning: an a* approach to path planning with consideration of variable vehicle speeds and multiple, overlapping, time-dependent exclusion zones. In Proceedings of the 1992 Symposium on Autonomous Underwater Vehicle Technology, 1992 (AUV '92), Huntsville, AL, pp. 79–84.
- Chow, B., Huissoon, J., & Clark, C. (2011). Assigning closely spaced targets to multiple autonomous underwater vehicles. *Journal of Ocean Technology*, 6(1), 57–77.
- Crimmins, D., Deacutis, C., Hinchey, E., Chintala, M., Cicchetti, G., & Blidberg, D. (2005, June). Use of a long endurance solar powered autonomous underwater vehicle (SAUV II) to measure dissolved oxygen concentrations in Greenwich Bay, Rhode Island, U.S.A. In Oceans 2005—Europe, Brest, France (Vol 2, pp. 896–901).
- Davini, B., Choboter, P., & Clark, C. (2011, August). Intelligent planning and assimilation of auv obtained measurements within a ROMS-based ocean modeling system. Paper presented at the International Symposium on Unmanned Untethered Submersible Technology (UUST), Portsmouth, NH.
- Dickey, T., Itsweire, E., Moline, M., & Perry, M. (2008). Introduction to the limnology and oceanography special issue on autonomous and Lagrangian platforms and sensors (ALPS). *Limnology and Oceanography*, 53, 2057–2061.
- Garcia, H., & Gordon, L. (1992). Oxygen solubility in sea water—better fitting equations. *Limnology and Oceanography*, 37, 1307–1312.
- Glud, R., Gundersen, J., & Ramsing, N. (2000). Electrochemical and optical oxygen microsensors for in situ measurements. In J. Buffle, G. Horval (Eds.), *In situ monitoring of aquatic systems: Chemical analysis and speciation* (pp. 20–73). New York: John Wiley & Sons.
- Grasmueck, M., Eberli, G., Correa, T., Viggiano, D. A., Luo, J., Wyatt, G., Reed, J., Wright, A., & Pompon, S. (2007). IAUV-based environmental characterization of deepwater coral mounds in the straits of Florida. In Offshore Technology Conference.
- Hume, H., Berg, P., & McGlathery, K. (2011). Dissolved oxygen fluxes and ecosystem metabolism in an eelgrass (*Zostera marina*) meadow measured with the eddy correlation technique. *Limnology and Oceanography*, 56, 86–96.
- Jenkins, A., Dutrieux, P., Jacobs, S. S., McPhail, S. D., Perrett, J. R., Webb, A. T., & White, D. (2010). Observations beneath Pine Island Glacier in west Antarctica and implications for its retreat. *Nature Geosci*, 3(7), 468–472.
- Johnson, K., & Needoba, J. (2008). Mapping the spatial variability of plankton metabolism using nitrate and oxygen sensors on an autonomous underwater vehicle. *Limnology and Oceanography*, 53, 2237–2250.
- Leonard, N., Paley, D., Lekien, F., Sepulchre, R., Fratantoni, D., & Davis, R. (2007). Collective motion, sensor networks, and ocean sampling. *Proceedings of the IEEE*, 95(1), 48–74.
- Moline, M., Bissett, P., Blackwell, S., Mueller, J., Sevdjian, J., Trees, C., & Zaneveld, R. (2005). An autonomous vehicle approach for quantifying bioluminescence in ports and harbors. In Proceedings SPIE International Society for Optical Engineering, Orlando, FL. (Vol. 5780 (13), pp. 81–87).
- Moline, M., Blackwell, S., Alt, C. V., Allen, B., Austin, T., Case, J., Forrester, N., Goldsborough, R., Purcell, M., & Stokey, R. (2005). Remote environmental monitoring units: An autonomous vehicle for characterizing coastal environments. *Journal of Atmospheric and Oceanic Technology*, 22, 1797–1808.
- Moline, M. A., Blackwell, S. M., Case, J. F., Haddock, S. H., Herren, C. M., Orrico, C. M., & Terrill, E. (2009).

- Bioluminescence to reveal structure and interaction of coastal planktonic communities. In John Milliman (Ed.), *Deep sea research, Part II. Topical studies in oceanography (AOSN II: The Science and Technology of an Autonomous Ocean Sampling Network)* (Vol. 56(3–5), pp. 232–245). Amsterdam: Elsevier.
- Nicholson, D., Emerson, S., & Eriksen, C. (2008). Net community production in the deep euphotic zone of the subtropical North Pacific gyre from glider surveys. *Limnology and Oceanography*, 53, 2226–2236.
- Petres, C., Pailhas, Y., Patron, P., Petillot, Y., Evans, J., & Lane, D. (2007). Path planning for autonomous underwater vehicles. *IEEE Transactions on Robotics*, 23(2), 331–341.
- Tengberg, A., Hovdenes, J., & Ersson, H., Brocandel, O., Diaz, R., Hebert, D., Arnerich, T., Huber, C., Kortzinger, A., Khrpounoff, A., Rey, F., Ronning, C., Schimanski, J., Sommer, S., & Stangelmayer, A. (2006, February). Evaluation of a lifetime-based optode to measure oxygen in aquatic systems. *Limnology and Oceanography—Methods*, 4, 7–17.
- Thrun, S., Burgard, W., & Fox, D. (2005). *Probabilistic robotics*. MIT Press.
- Uchida, H., Kawano, T., Kaneko, I., & Fukasawa, M. (2008). In situ calibration of optode-based oxygen sensors. *Atmospheric and Oceanic Technology*, 25, 2271–2281.
- Wang, D. (2007). *Autonomous underwater vehicle (AUV) path planning and adaptive on-board routing for adaptive rapid environmental assessment*. Ph.D. thesis, Massachusetts Institute of Technology (MIT) Cambridge, MA. [AAI0819974].
- Webb, D., Simonetti, P., & Jones, C. (2001). Slocum: An underwater glider propelled by environmental energy. *IEEE Journal of Oceanic Engineering*, 26(4), 447–452.
- Williams, S., Pizarro, O., Jakuba, M., & Barrett, N. (2010). AUV benthic habitat mapping in south eastern Tasmania. In A. Howard, K. Iagnemma, and A. Kelly, (eds.), *Field and service robotics, Springer tracts in advanced robotics* (Vol. 62, pp. 275–284). Berlin/Heidelberg: Springer.